

Spectroscopical Confirmation and Lens Modeling of a Complex Strong Lensing System Produced by a Close Galaxy Pair at $z_d = 0.79$

ZIZHAO HE ^{1,2,3} LIMENG DENG ^{3,4} QIHANG CHEN ^{5,6} YIPING SHU ³ NAN LI ⁷ AND DI WU ^{7,8}

¹*Department of Physics, Nanchang University, Nanchang, 330031, China*

²*Center for Relativistic Astrophysics and High Energy Physics, Nanchang University, Nanchang, 330031, China*

³*Purple Mountain Observatory, Chinese Academy of Sciences, Nanjing, Jiangsu, 210023, China*

⁴*School of Astronomy and Space Sciences, University of Science and Technology of China, Hefei 230026*

⁵*School of Physics and Astronomy, Beijing Normal University, Beijing, 100875, China*

⁶*Institute for Frontier in Astronomy and Astrophysics, Beijing Normal University, Beijing, 102206, China*

⁷*National Astronomical Observatories, CAS, Beijing 100101, China*

⁸*School of Astronomy and Space Science, University of Chinese Academy of Sciences, Beijing 100049, China*

ABSTRACT

We report the spectroscopic confirmation and lens modeling of the complex strong-lens system J0233–0205, in which the deflector consists of a pair of galaxies at $z_d = 0.790 \pm 0.022$, the background source lies at $z_s = 2.160 \pm 0.002$, and the circularized Einstein radius is $\theta_E = 1''.680 \pm 0''.003$. Our lens modeling requires two lens components—two elliptical galaxies with Einstein radii of $0''.669 \pm 0''.002$ and $0''.735 \pm 0''.002$, respectively, and a projected separation of $0''.513$ (~ 3.832 kpc)—as well as three source components: two disk galaxies separated by $0''.4965$ (~ 3.712 kpc), plus a point-like component closely aligned with one of the disks. From a joint lensing and stellar-population analysis, we infer a total stellar mass within the critical curve of the lens pair of $M_{*,\text{total}} = (1.956 \pm 0.418) \times 10^{11} M_\odot$ and a total enclosed mass of $M_{\text{lensing},\text{total}} = (1.107 \pm 0.008) \times 10^{12} M_\odot$, corresponding to a projected dark-matter fraction of $f_{\text{dm}} = 82 \pm 4\%$. The stellar masses of the two lens galaxies are $M_{*,\text{lens1}} = (8.548 \pm 2.128) \times 10^{10} M_\odot$ and $M_{*,\text{lens2}} = (1.525 \pm 0.295) \times 10^{11} M_\odot$, implying dark-matter fractions within the z -band effective radius of $57 \pm 11\%$ and $70 \pm 6\%$, respectively. The small separation of the lens pair, together with its relatively high deflector redshift, makes J0233–0205 a potentially ideal laboratory for probing the mass distribution and dark-matter content of close galaxy pairs. In addition, the two disk galaxies and the associated point-like source make this system valuable for investigating the merger process in the source plane.

Keywords: gravitational lensing: strong – galaxies: elliptical and lenticular, cD – galaxies: interactions – galaxies: pairs – galaxies: structure

1. INTRODUCTION

Strong gravitational lensing provides one of the most direct and precise means of probing galaxy mass distributions on kiloparsec scales. By modeling the relative positions, shapes, and surface-brightness morphologies of lensed images, one can robustly infer the projected total mass enclosed within the Einstein radius and tightly constrain the geometry of the lensing potential (L. V. E. Koopmans et al. 2006; T. Treu 2010; G. Granata et al. 2023). At the same time, lensing magnification acts as a natural telescope: it boosts the apparent flux and enhances the effective source-plane spatial resolution, enabling the detection and spatially resolved characterization of intrinsically fainter galaxies (A. M. Swinbank et al. 2007; T. A. Jones et al. 2010; X. Er et al. 2013; P. Natarajan et al. 2024).

In galaxy–galaxy strong lensing, the deflectors are most commonly luminous red galaxies (LRGs) with stellar masses of $M_* \sim 10^{10}$ – $10^{12} M_\odot$ (Y. Shu et al. 2017), while the sources are typically extended, star-forming galaxies with young stellar populations (e.g., Z. He et al. 2020; R. Li et al. 2021; X. Huang et al. 2021). Large samples of such systems have shown that the total (stars + dark matter) projected mass profile within $\sim \theta_E$ is often close to isothermal. These samples have therefore become a cornerstone for investigating the redshift evolution of mass-density slopes and for placing cosmological constraints (e.g., A. S. Bolton et al. 2012; R. Li et al. 2018; W. Sheu et al. 2025; S. Geng et al.

2025; E. L. Turner et al. 1984; K.-H. Chae et al. 2002; M. Oguri et al. 2012; T. Li et al. 2024). On larger scales, strong lensing by galaxy clusters provides complementary insights into mass distributions on ~ 100 kpc scales, revealing the interplay between dark matter, baryons, and dynamical assembly in massive halos (J.-P. Kneib & P. Natarajan 2011; M. Meneghetti et al. 2020; P. Natarajan et al. 2024). Despite this progress, several key questions remain central to lensing-based studies of galaxy structure. In particular, the mass distribution in *close galaxy pair*—systems in which galaxies are separated by $\sim 1\text{--}50$ kpc—remains poorly constrained, and such systems provide a sensitive probe of the collisional nature of dark matter (see, e.g., C. R. Keeton & J. N. Winn 2003; C. Grillo & L. Christensen 2011; Y. Shu et al. 2016).

The system J0233–0205 was first identified as a grade-A strong-lens candidate (A. T. Jaelani et al. 2020) in Hyper Suprime-Cam Subaru Strategic Program imaging (HSC-SSP; H. Aihara et al. 2018) by the Survey of Gravitationally Lensed Objects in HSC Imaging (SuGOHI; A. Sonnenfeld et al. 2018). It drew our attention because the imaging shows bright point-like emission accompanied by two highly distorted arcs in an offset configuration, suggestive of a rich, multi-component lensing geometry. Motivated by its unusual morphology, we conducted a detailed follow-up investigation and found that both the light distribution and the lensing configuration favor two distinct deflector components, while the source plane contains three clearly separated components (two galaxies plus one point-like source).

J0233–0205 provides a unique laboratory to address these questions. First, the two galaxies acting as deflectors are separated by only $\sim 0''.5$ (corresponding to ~ 4 kpc at $z_d = 0.790 \pm 0.022$), offering a rare opportunity to probe the total mass distribution in an interacting, compact configuration at a cosmic time of ~ 6.5 Gyr. Second, the background source is strongly magnified (by a factor of $\sim 10\text{--}20$), enabling a detailed view of intrinsically faint structures. The lensed emission originates from a merging disk-galaxy system associated with a compact Ly α emitter at cosmic noon ($z_s = 2.160 \pm 0.002$). Together, these properties make J0233–0205 an exceptional case for testing how galaxy–galaxy interactions reshape the inner total-mass profile and the relative contributions of stars and dark matter on kiloparsec scales.

We obtained spectroscopic observations in September 2023 using the Palomar 200-inch Double Beam Spectrograph (P200/DBSP), which confirm the lensing interpretation by identifying the lens and source redshifts. We then carried out a joint analysis combining spectroscopic measurements, multi-component lens modeling, and spectral energy distribution (SED) fitting to comprehensively characterize both the deflectors and the sources, and to connect the lensing-inferred total mass distribution to the stellar-mass content of the deflectors.

This paper is organized as follows. Section 2 describes the data sets used, including both imaging and spectroscopic observations. Section 3 presents the analysis of the spectroscopic data. Section 4 details the lens-modeling methodology and results. Section 5 combines our lensing constraints with stellar population synthesis (SPS) modeling to measure the dark-matter fraction of the lens galaxies, and compares our results with previous measurements in the literature. Section 6 summarizes the main findings of the paper. Throughout this paper, we adopt a fiducial cosmology with $\Omega_m = 0.3$, $\Omega_{DE} = 0.7$, $h = 0.7$, $w_0 = -1$, and $w_a = 0$. In this cosmology, $1''$ corresponds to ~ 7.476 kpc at $z_d = 0.79$. Unless otherwise stated, all magnitudes are reported in the AB system.

2. DATA

We use both public available imaging data from HSC-SSP third public data release (HSC-SSP PDR3, H. Aihara et al. 2022), and the private spectroscopy resources of Palomar 200-inch Double Beam Spectrograph (P200 DBSP, J. B. Oke & J. E. Gunn 1982) in California. Here, we give an introduction of those data we utilized.

2.1. Imaging Data

The image data used for this work was collected from the Wide layer of the HSC-SSP PDR3. Generally speaking, the Wide layer covers 670 deg^2 of sky that have simultaneous detections in five filters: g , r , i , z , and y . The median seeing values are $0''.79$, $0''.75$, $0''.61$, $0''.68$, and $0''.68$ for the g , r , i , z , and y bands, respectively. The 5σ depths for point sources in the Wide layer are $g = 26.5$, $r = 26.5$, $i = 26.2$, $z = 25.2$, and $y = 24.4$ (H. Aihara et al. 2022).

The image cutout used in this study has a size of 39×39 pixels ($6''.55 \times 6''.55$), centered at RA = 38.34375° , Dec = -2.09190° , with each pixel corresponding to $0''.168$. The cutout is obtained using the web query ‘DAS Cutout’⁹

⁹ https://hsc-release.mtk.nao.ac.jp/das_cutout/pdr3/

. Using these coordinates, we employed the ‘PSF Picker’ tool¹⁰ to generate PSF models for all bands of the HSC survey, as part of the Wide Field Survey described in H. Aihara et al. (2018).

2.2. Spectra Data

We observed this target with the Double Spectrograph (DBSP) on the 200-inch Hale Telescope (P200; P.I. Zizhao He) on 2023 October 15–16. On the first night (October 15), we set the slit position angle to 0° to cover only image B, as illustrated in the left-hand panel of the top row of Figure 1. On the second night (October 16), the slit was rotated to pass through both images A and B as well as the intervening red component, as shown in the right-hand panel of the second row of Figure 1. On both nights, the target was exposed for 1800s and used a slit width of $1''.5$. We used the standard D-55 dichroic to split the light into blue and red channels. The blue arm employed the 300 line mm^{-1} grating blazed at $\sim 3990\text{\AA}$, and the red arm used the 316 line mm^{-1} grating blazed at $\sim 7150\text{\AA}$, providing dispersions of 2.108\AA and $1.535\text{\AA}\text{ pixel}^{-1}$ for the blue and red arms, respectively (J. B. Oke & J. E. Gunn 1982).

The raw spectra were reduced with a PYTHON¹¹ module, PySpecRedux, that we developed, which builds on standard astronomical packages: Astropy (Astropy Collaboration et al. 2022), NumPy (C. R. Harris et al. 2020), Pandas (Wes McKinney 2010), and SciPy (P. Virtanen et al. 2020). The reduction followed standard procedures, including bias subtraction, flat-fielding, cosmic-ray rejection with Astrocrappy (C. McCully et al. 2018), one-dimensional spectrum extraction, and wavelength and flux calibration. For further details, we refer the reader to Section 2.3 of Z. He et al. (2025).

The processed spectra are presented in the 2nd to 4th row of Figure 1. The second row shows the spectrum of image B from October 15, the third row shows the spectrum of image A from October 16, and the fourth row shows the spectrum of image B from October 16.

Table 1. HSC photometric-redshift estimates information for the lens galaxies.

Quantity	Value
object_id	39627245173625540
R.A. ($^\circ$)	38.3444
Dec. ($^\circ$)	-2.0918
photoz_best_dmnz	0.720
photoz_std_best_dnnz	0.546
photoz_mode_demp	0.700
photoz_std_mode_demp	0.107
photoz_best_mizuki	0.790
photoz_std_best_mizuki	0.048

Notes: We list the photometric-redshift (z_{phot}) point estimates and their corresponding 1σ uncertainties provided by HSC PDR3 for all three photo- z algorithms (see M. Tanaka et al. 2018; A. J. Nishizawa et al. 2020, for details). For the DEmP method, following the official recommendation^a, we adopt the ‘mode’ estimate rather than the ‘best’ estimate. Values highlighted in bold indicate the smallest uncertainty among the three methods. Note that the two lens galaxies were treated as a single source in PDR3 (with the object_id listed above).

^ahttps://hsc-release.mtk.nao.ac.jp/doc/wp-content/uploads/2022/08/pdr3_photoz.pdf

3. SPECTROSCOPIC ANALYSES

As shown in Figure 1, a direct comparison of the spectra of images A and B from October 16 reveals a high degree of similarity. Both spectra exhibit the same set of emission features at the $z_s = 2.160 \pm 0.001$, including $\text{Ly}\alpha$, S_{IV} , C_{IV} , and Mg_{II} . This provides strong spectroscopic evidence that images A and B are multiple images of the same background galaxy, and thus supports the lensing interpretation for this system.

We measure the redshifts of the lens galaxies via template fitting, as shown in Figure 2. To maximize the contribution from the lens light, we use the spectrum of image A obtained on October 16 (fourth row of Figure 1). Because image A lies closer to the lens galaxies than image B, its extracted spectrum contains a larger fraction of lens-galaxy light.

¹⁰ <https://hsc-release.mtk.nao.ac.jp/psf/pdr3/>

¹¹ <https://www.python.org/>

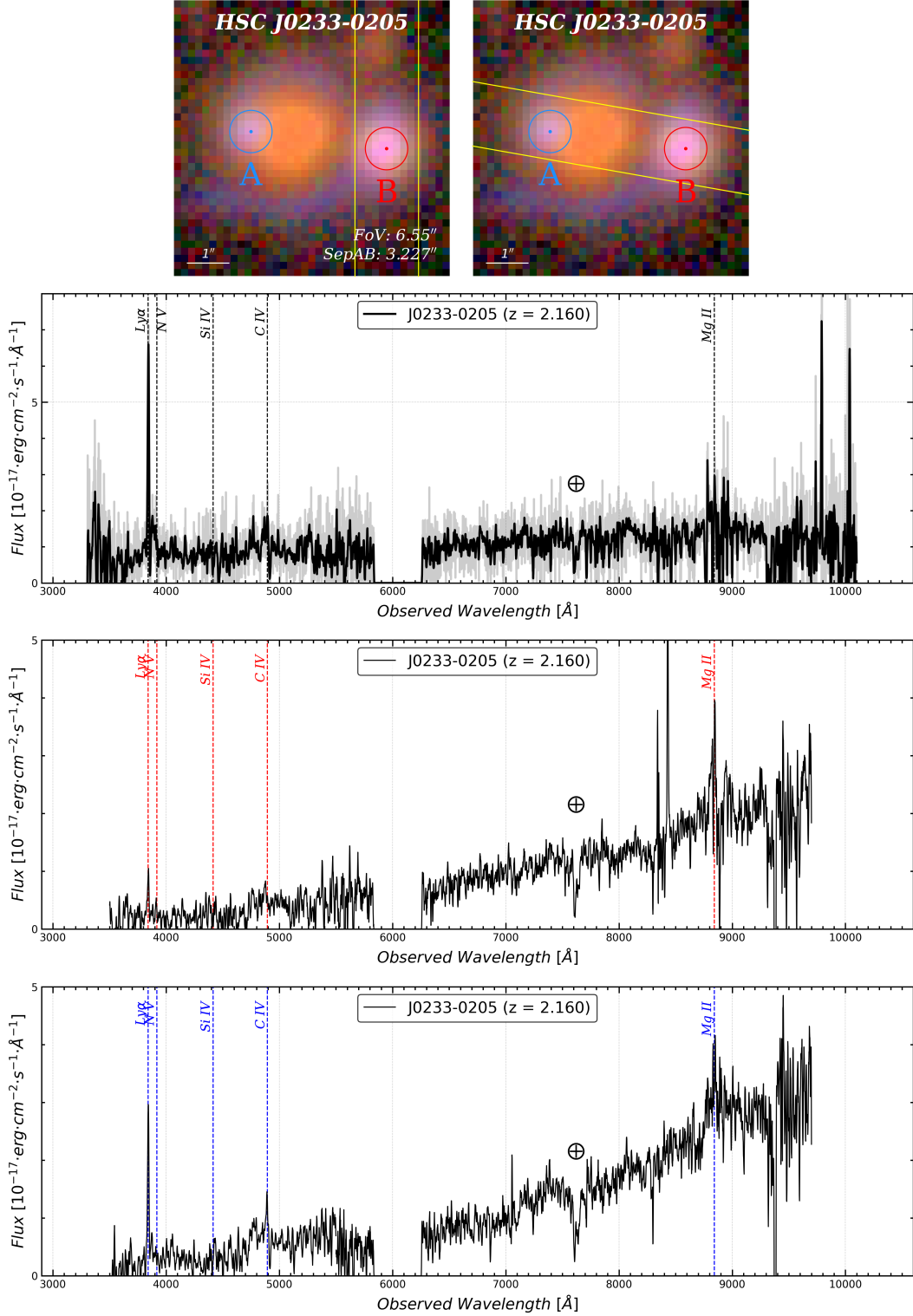


Figure 1. Spectroscopic follow-up of HSC J0233–0205 with P200/DBSP. **Top row:** RGB cutouts showing the DBSP slit placements for the two exposures (Oct. 15: left; Oct. 16: right). North is up and east is to the left. The lensed compact galaxies A (blue) and B (red) are marked, and the scale bar (1") and image separation (3".20) are indicated; yellow lines outline the slit. **Second row:** 1D spectrum extracted from image B in the Oct. 15 exposure. **Third row:** 1D spectrum extracted from image A in the Oct. 16 exposure. Vertical dashed lines mark prominent emission features (Ly α , Si IV, C IV, and Mg II) at the derived source redshift, and the \oplus symbol denotes a telluric absorption band. From these spectra, we measure $z_s = 2.160 \pm 0.001$.

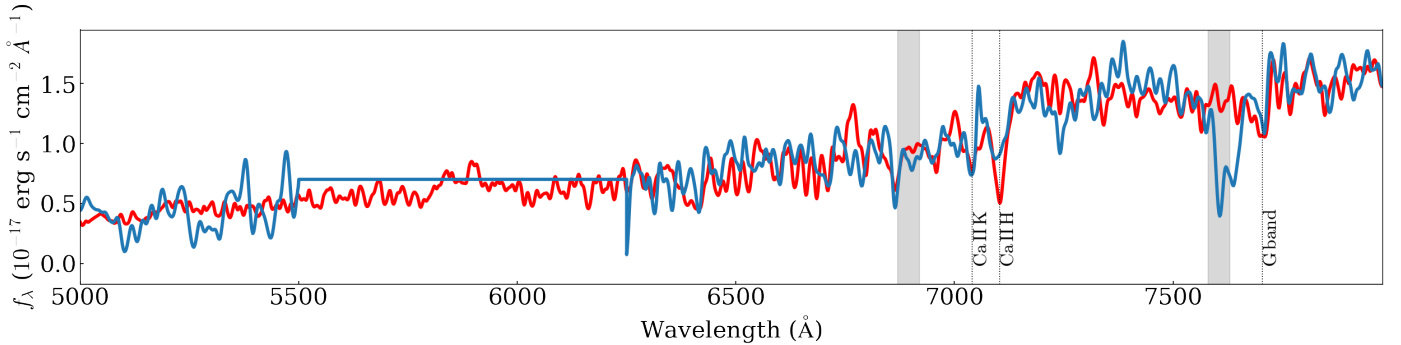


Figure 2. Optical spectrum of the lens galaxies in HSC J0233–0205, showing a secure redshift of $z_d = 0.790 \pm 0.022$. The blue curve shows the observed spectrum, while the red curve shows the best-fitting template spectrum. The dotted vertical lines mark the expected observed wavelengths of prominent stellar absorption features at this redshift (e.g., Ca H&K, G band, Mg, and Balmer lines), and the gray shaded regions indicate wavelength intervals strongly affected by atmospheric/telluric absorption (and thus masked in the fit).

We fit the lens-galaxy spectrum within the observed wavelength range of 3700–8000Å using a linear combination of galaxy spectral templates generated by [T. A. Hutchinson et al. \(2016\)](#), with the template coefficients determined through a standard linear least-squares fit. During the fit, we mask both the background-source emission lines (Ly α , Nv, SiIV, and CIV) and the telluric (atmospheric) absorption bands, highlighted by the gray shaded regions in Figure 2. Although the fit is performed over 3700–8000Å, only the 5000–8000Å range is displayed in Figure 2 for visual clarity. The best-fitting redshift is $z_d = 0.790 \pm 0.022$, and the model reproduces prominent absorption features such as Ca II H&K and the G band. This value is consistent with the photometric redshift reported in the HSC DR3 catalog ($z_{d,\text{phot}} = 0.790 \pm 0.048$), as listed in the last two rows of Table 1.

4. STRONG LENS MODELING

From the spectral analysis presented above, we confirm the lensing nature of HSC J0233–0205. Lens modeling is then required to infer the physical properties of both the deflector(s) and the source(s). Here we describe our modeling methodology and present the corresponding results. Throughout the modeling, we adopt the reference position (R.A., Dec.) = (38.344221°, –2.091836°), and all (x, y) coordinates are measured relative to this point.

4.1. Model set-up

We modeled the multi-band HSC imaging of HSC J0233–0205 with `lenstronomy` ([S. Birrer & A. Amara 2018](#)) to measure the strong-lensing parameters of the system, together with the positions and magnitudes of the lens galaxies and lensed images. We adopted a two-EPL mass models to represent two deflectors, respectively. For a single EPL component, the surface mass density is given by

$$\Sigma(x, y) = \Sigma_{\text{crit}} \frac{3 - \gamma_{\text{EPL}}}{2} \left(\frac{\theta_{\text{E}}}{\sqrt{q_{\text{EPL}} x^2 + y^2/q_{\text{EPL}}}} \right)^{\gamma_{\text{EPL}} - 1}, \quad (1)$$

where θ_{E} is the Einstein radius, γ_{EPL} is the logarithmic slope of the projected density profile, q_{EPL} is the minor-to-major axis ratio, (x, y) are Cartesian coordinates aligned with the major and minor axes of the mass distribution, and Σ_{crit} is the critical surface density, $\Sigma_{\text{crit}} = (c^2/4\pi G) (D_S/D_L D_{LS})$.

For the lens light, we model the two deflector galaxies with two Sérsic components, each sharing its centroid with the corresponding EPL mass component. Each Sérsic profile is parameterized by the effective radius (r_e), axis ratio (q_s), position angle (ϕ_s), centroid coordinates (x_c, y_c), and the total magnitude (m). For both galaxies, we fix the Sérsic index to $n_s = 4$, i.e., a de Vaucouleurs profile appropriate for massive early-type galaxies. With seeing-limited ground-based imaging, the two lens components are only marginally resolved, and their individual Sérsic indices cannot be robustly constrained. This assumption is commonly adopted in strong-lensing analyses of early-type galaxies and in multi-band structural studies, which typically find only weak wavelength dependence of n_s for such systems (e.g., [A. S. Bolton et al. 2008](#); [B. Vulcani et al. 2014](#); [V. Marian et al. 2018](#)). During the fit, we tie the structural parameters (x_c, y_c, ϕ_s, q_s) across all bands, allowing only m and r_e to vary with wavelength.

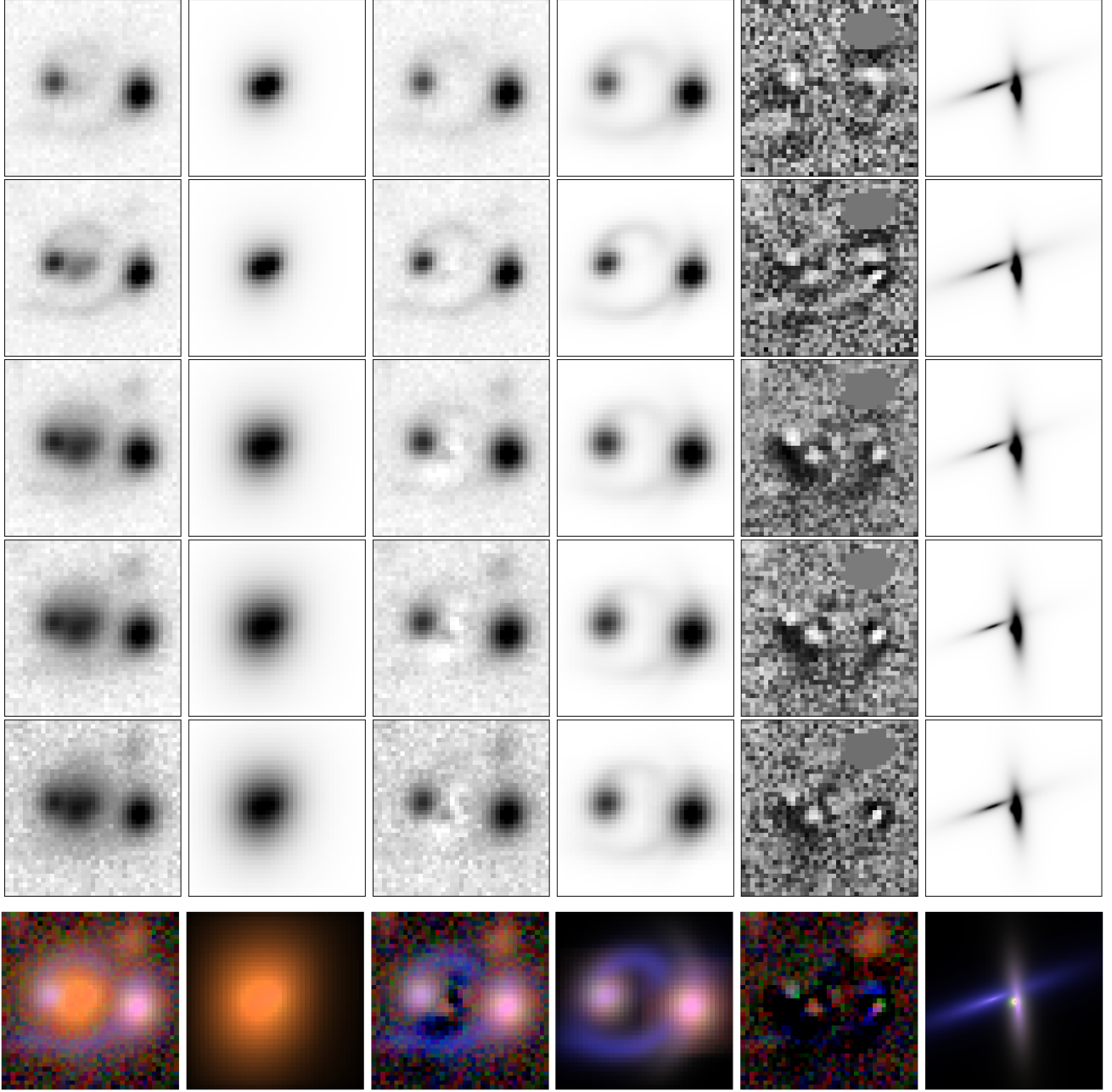


Figure 3. Best-fitting results. North is up and east is to the left. From left to right, the six columns show the data, the lens-light model, the lens-light-subtracted data, the lensed-image model, the residual, and the source-light model. The first five rows correspond to the g , r , i , z , and y bands, respectively, and the last row shows a color-composite image generated from all five bands. The first five columns cover $6''.55 \times 6''.55$ with a pixel scale of $0''.168$, while the last column covers $3'' \times 3''$ with a pixel scale of $0''.168$. In the last row, the residual panel shows the unnormalized residual (data – model), whereas the other rows show normalized residuals.

For the source light, we represent the source-plane emission with three Sérsic components: two extended galaxies and one compact component. For the compact component, we fix $n_s = 4$, $\phi_s = 0$ and $q_s = 1$, and impose a tight prior on its size, $0''.001 < r_e < 0''.01$, to enforce a nearly unresolved morphology (i.e., a point-like source). For the two extended source galaxies, we tie the structural parameters (x_c , y_c , q_s , ϕ_s) across all bands, while allowing m , r_e , and n_s to vary with wavelength. We leave n_s free because the HSC filters sample different rest-frame wavelengths for

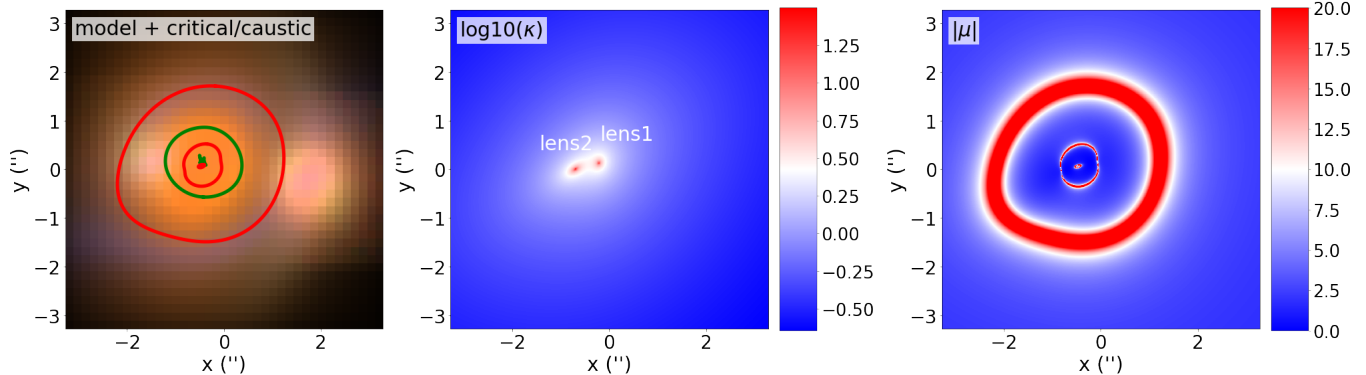


Figure 4. Visualization of the best-fitting lens model. North is up and east is to the left. **Left:** RGB composite of the modeled lensed image in the image plane, overlaid with the model-predicted critical curves (red) and caustics (green). **Middle:** dimensionless convergence map, κ , for the total mass model; the labeled markers indicate the positions of the two lens components (lens1 and lens2). **Right:** lensing magnification map shown as the absolute magnification, $|\mu|$. All three panels cover the same field of view, $6''.55 \times 6''.55$, and share the same coordinate system, with axes labeled in arcseconds. The middle and right panels are displayed with a pixel scale of $0''.0168$ per pixel. Color bars indicate the corresponding values of κ and $|\mu|$.

these star-forming sources, whose apparent morphologies can exhibit stronger wavelength dependence than those of the early-type deflectors.

4.2. Results

The fitting results are summarized in Table 2 (mass model), Table 3 (lens light), and Table 4 (source light). The band-by-band modeling results, together with the corresponding five-band composite color images, are presented in Figure 3. The best-fitting lens model is shown in Figure 4. Overall, our model reproduces the imaging data well, with a reduced χ^2 of 1.4913. Compared to S. Schuldt et al. (2023), which modeled this system with a semi-automated modeling pipeline based on GLEE (S. H. Suyu 2012), our normalized-residual maps appear less structured and show no prominent ring-like features. Our fit quality is also improved, yielding a lower reduced χ^2 of 1.4913 compared to 1.87 in S. Schuldt et al. 2023, despite a comparable level of model complexity, with both analyses employing two lens components and three source components.

4.2.1. Mass Model

The best-fitting power-law slopes are $\gamma_{\text{EPL}} = 1.758$ and 1.833 , both slightly shallower than the isothermal case ($\gamma_{\text{EPL}} = 2$), implying a somewhat more extended total mass distribution. Nevertheless, these values lie well within the typical scatter of the nearly isothermal profiles commonly inferred for galaxy-scale strong lenses (see, e.g., R. Li et al. 2018; S. Geng et al. 2025). The best-fit Einstein radii are $\theta_E = 0''.669 \pm 0''.002$ and $0''.735 \pm 0''.002$ for lens1 and lens2, respectively, indicating that lens2 is modestly more massive than lens1.

We further compute a circularized Einstein radius for the overall system of $\theta_E = 1''.680 \pm 0''.003$. Based on the area enclosed by the critical curve, we derive the projected mass enclosed by the critical curve directly from the model convergence map (middle panel of Figure 4). We obtain a mass enclosed within the critical curve of $M_{\text{lensing, total}} = (1.107 \pm 0.008) \times 10^{12} M_{\odot}$.

4.2.2. Lens Light

The best-fitting parameters of lens light are summarized in Table 3, while the second column of Figure 3 shows the model images of two lenses. Sérsic 1 is located at $(x_c, y_c) = (-0''.217, 0''.129)$ with respect to the coordinate origin, and it has a position angle $\phi_s \simeq 65.4$ and an axis ratio $q_s \simeq 0.57$, indicating a moderately flattened early-type galaxy. The effective radius lies in the range $r_e \simeq 0''.34\text{--}0''.45$, corresponding to $r_e \simeq 2.58\text{--}3.34$ kpc $z_d = 0.79$. Sérsic 2 represents the secondary lens galaxy, centered at $(x_c, y_c) = (-0''.697, 0''.002)$ with a nearly vertical major axis ($\phi_s \simeq 88.3$) and $q_s \simeq 0.73$. Its effective radius is larger, $r_e \simeq 0''.63\text{--}0''.89$ or $r_e \simeq 4.73\text{--}6.66$ kpc, again typical of a massive early-type system.

In addition, the two deflectors exhibit very similar optical colors in the multi-band imaging (Figure 3), this close similarity suggests that Sérsic1 and Sérsic2 are likely at the same (or very similar) redshift, consistent with a physically associated lens pair rather than a chance superposition along the line of sight.

Table 2. Best-fitting parameters of the EPL mass models.

Comp	θ_E (")	γ_{EPL}	ϕ_{EPL} (°)	q_{EPL}	$\gamma_{\text{shear},1}$	$\gamma_{\text{shear},2}$
Lens1	0.669 ± 0.002	1.758 ± 0.006	68.426 ± 0.041	0.843 ± 0.010	0.019 ± 0.003	0.123 ± 0.003
Lens2	0.735 ± 0.002	1.833 ± 0.006	32.102 ± 0.013	0.582 ± 0.008		

Notes: The lens mass centroids are fixed to the corresponding Sérsic light centroids (Table 3) and are therefore not listed here. Position angles are measured from the $+x$ axis, with $\phi = 0^\circ$ aligned with $+x$ and increasing counterclockwise.

Table 3. Lens light parameters

Comp	Band	m	Center x (")	Center y (")	ϕ_s (°)	q_s	r_e (")	n_s
Sersic 1	g	24.140 ± 0.029					0.345 ± 0.001	4.000
	r	23.010 ± 0.026					0.447 ± 0.001	4.000
	i	21.629 ± 0.018	-0.217 ± 0.001	0.129 ± 0.001	65.389 ± 0.478	0.573 ± 0.006	0.446 ± 0.001	4.000
	z	21.012 ± 0.018					0.426 ± 0.002	4.000
	y	20.756 ± 0.016					0.420 ± 0.002	4.000
Sersic 2	g	24.098 ± 0.074					0.633 ± 0.001	4.000
	r	22.651 ± 0.047					0.840 ± 0.002	4.000
	i	21.183 ± 0.019	-0.697 ± 0.001	0.002 ± 0.001	88.365 ± 0.550	0.737 ± 0.007	0.868 ± 0.002	4.000
	z	20.669 ± 0.018					0.891 ± 0.001	4.000
	y	20.217 ± 0.016					0.820 ± 0.002	4.000

Notes: The Sérsic components represent the two lens galaxies, modeled independently in each HSC band. For each component, the centroid (x, y) , position angle ϕ_s , and axis ratio q_s are tied across all bands, while the magnitude m and effective radius r_e are allowed to vary with wavelength. The Sérsic index is fixed to $n_s = 4$ for both components. Position angles are measured from the $+x$ axis, with $\phi_s = 0^\circ$ aligned with $+x$ and increasing counterclockwise. The coordinate origin is defined in the image plane (see text for details).

4.2.3. Source Light

The best-fitting source-light parameters are summarized in Table 4, including the absolute lensing magnification. The magnification for each source component is estimated by comparing its total flux measured in the image plane to that in the reconstructed source plane.

Sérsic1 corresponds to the more extended and slightly fainter (but more strongly magnified) component, with $r_e \simeq 0''.29\text{--}0''.85$ (2.13–6.35 kpc) and a Sérsic index of $n_s \simeq 4$, indicative of a moderately concentrated profile. Its lensing magnification is $\mu \simeq 21.4\text{--}24.9$. It is also highly flattened, with an axis ratio of $q_s \simeq 0.152$, suggesting a strongly elongated morphology (e.g., an edge-on disk or a tidally distorted structure). Sérsic2 is more compact, with $r_e \simeq 0''.05\text{--}0''.11$ (0.37–0.83 kpc) and a higher Sérsic index of $n_s \simeq 5$. It is magnified by $\mu \simeq 9.7\text{--}11.9$. Compared to Sérsic1, it is substantially rounder, with $q_s \simeq 0.262$, and it becomes progressively brighter than Sérsic1 toward redder bands, suggesting a older stellar population and a more centrally concentrated light distribution. Sérsic3 is consistent with a point-like component, with a more modest magnification of $\mu \simeq 6.0\text{--}7.4$. Its color is very similar to that of Sérsic2, and the centroid separation between the two components is only $0''.041 \pm 0''.0014$ (corresponding to 0.308 ± 0.011 kpc), suggesting that Sérsic3 plausibly traces a compact knot near the center of Sérsic2 (e.g., a nuclear star-forming clump or an unresolved central component).

The rightmost column of Figure 3 presents the reconstructed source-plane images of these components in each HSC band. Based on these reconstructions, we argue that the background source is likely a merging system consisting of two interacting galaxies: one primarily described by the highly elongated Sérsic1 component, and the other represented by the more compact (and comparatively rounder) Sérsic2 plus Sérsic3.

5. DISCUSSION

5.1. Stellar-population and Dark Matter Fraction

To estimate the stellar masses of the lens galaxies, we perform SED fitting with CIGALE (M. Boquien et al. 2019), assuming a Chabrier IMF (G. Chabrier 2003). We adopt a metallicity grid of $Z = 0.0004, 0.004, 0.008, 0.02, \text{ and } 0.05$,

Table 4. Source light parameters

Band	m	Center x (")	Center y (")	ϕ_s (°)	q_s	r_e (")	n_s	μ
Sersic 1								
g	24.836 ± 0.030					0.404 ± 0.002	3.071 ± 0.008	22.110
r	26.373 ± 0.042					0.850 ± 0.002	3.916 ± 0.007	21.382
i	25.963 ± 0.174	-0.360 ± 0.001	0.026 ± 0.001	0.338 ± 0.002	0.152 ± 0.002	0.426 ± 0.003	3.824 ± 0.007	22.997
z	25.548 ± 0.278					0.286 ± 0.002	4.162 ± 0.006	24.960
y	25.606 ± 0.164					0.463 ± 0.002	4.023 ± 0.007	22.983
Sersic 2								
g	24.278 ± 0.101					0.111 ± 0.002	5.230 ± 0.007	10.148
r	21.819 ± 0.201					0.050 ± 0.002	3.096 ± 0.008	9.699
i	22.536 ± 0.146	0.058 ± 0.001	-0.030 ± 0.001	178.526 ± 0.003	0.262 ± 0.002	0.089 ± 0.002	5.116 ± 0.007	10.470
z	21.669 ± 0.156					0.072 ± 0.002	5.401 ± 0.007	11.199
y	21.268 ± 0.185					0.060 ± 0.002	5.409 ± 0.007	11.975
Sersic 3								
g	23.817 ± 0.240					0.005	4.000	7.002
r	22.972 ± 0.260					0.004	4.000	6.743
i	23.131 ± 0.274	0.020 ± 0.001	-0.014 ± 0.001	0.000	1.000	0.006	4.000	7.422
z	21.930 ± 0.274					0.004	4.000	6.908
y	21.414 ± 0.386					0.004	4.000	6.578

Notes: The source is modeled with three Sérsic components in the reconstructed source plane. For each component, the centroid (x, y) , position angle ϕ_s , and axis ratio q_s are tied across all bands, while the magnitude m , effective radius r_e , and Sérsic index n_s are fitted independently in each band (except for Sérsic 3, for which n_s is fixed to 4). Sérsic 3 has $q_s = 1$ and a very small r_e , and thus effectively represents a point-like source component. The magnification factor μ is computed from the best-fitting lens model for each band (see text for details). Position angles are measured from the $+x$ axis, with $\phi_s = 0^\circ$ aligned with $+x$ and increasing counterclockwise.

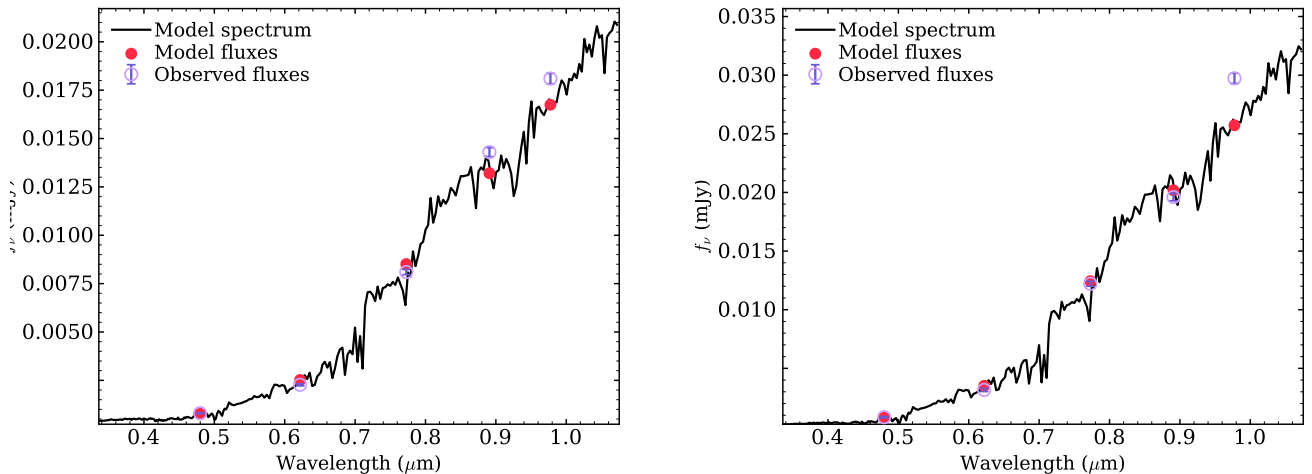


Figure 5. CIGALE SED fitting result. Open and filled circles correspond to the observed and model-predicted photometry.

and use the BC03 single-stellar-population models (G. Bruzual & S. Charlot 2003). The star formation history is modeled with a double-exponential form (`sfh2exp`), while dust attenuation is described using the `dustatt_modified_CF00` module (S. Charlot & S. M. Fall 2000). This setup is applied to the observed five-band HSC photometry of the two lens galaxies, and the best-fitting SED models are shown in Figure 5. The resulting Bayesian stellar-mass estimates are $M_{*,\text{lens1}} = (8.548 \pm 2.128) \times 10^{10} M_\odot$ and $M_{*,\text{lens2}} = (1.525 \pm 0.295) \times 10^{11} M_\odot$. Taking their sizes into account

Table 5. Enclosed mass budget and dark-matter fraction within different circular apertures. Masses are reported in units of $10^{11} M_{\odot}$. The dark-matter fraction is given in percent.

Lens	Aperture	Band	r_{ap} (arcsec)	f_{\star}	$M_{\text{lensing}}(< r_{\text{ap}})$ ($10^{11} M_{\odot}$)	$M_{\star}(< r_{\text{ap}})$ ($10^{11} M_{\odot}$)	f_{DM} (%)
lens1	r_e	z	0.426	0.500	0.987 ± 0.005	0.427 ± 0.106	56.7 ± 10.8
lens2	r_e	z	0.891	0.500	2.572 ± 0.007	0.762 ± 0.148	70.4 ± 5.7
lens1	$r_e/2$	z	0.213	0.320	0.417 ± 0.003	0.273 ± 0.068	34.5 ± 16.3
lens2	$r_e/2$	z	0.446	0.320	1.146 ± 0.005	0.488 ± 0.094	57.4 ± 8.3
lens1	θ_E	-	0.669	0.625	1.730 ± 0.004	0.535 ± 0.133	69.1 ± 7.7
lens2	θ_E	-	0.735	0.447	2.055 ± 0.005	0.682 ± 0.132	66.8 ± 6.4

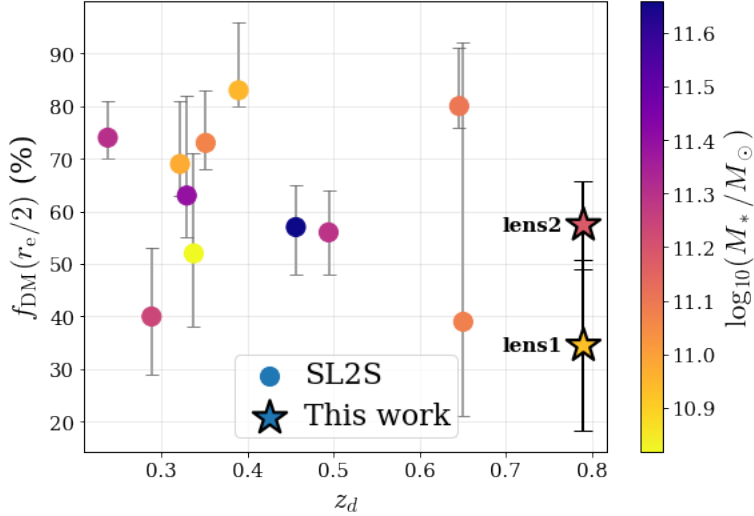


Figure 6. Comparison of projected dark-matter fractions within the z -band effective radius r_e as a function of deflector redshift. The two lens galaxies in HSC J0233–0205 are highlighted, while the literature sample is shown for reference.

(see Section 4.2.2), we find that both lens galaxies are consistent with the size–mass relation of early-type galaxies at $z \simeq 0.75$ (see Figure 5 and Table 1 of A. vanderWel et al. 2014).

We then estimate the stellar mass enclosed by the critical curve. Specifically, we integrate the lens-galaxy light within the critical curve and compute its flux ratio relative to the total model flux of Sérsic Lens1+Lens2, denoted as $f_{\star, \text{crit}}$. Assuming that stellar mass traces the observed light, we estimate the enclosed stellar mass as

$$M_{\star, \text{crit}} = f_{\star, \text{crit}} \times (M_{\star, \text{lens1}} + M_{\star, \text{lens2}}). \quad (2)$$

The calculation returns $f_{\star, \text{crit}} = 0.822$, which yields $M_{\star, \text{crit}} = (1.956 \pm 0.418) \times 10^{11} M_{\odot}$. Combining these with the lensing mass, $M_{\text{lensing, total}}$, derived in Section 4, we infer a projected dark-matter fraction within the critical curve of $82 \pm 4\%$.

To estimate the dark-matter fraction, f_{dm} , of each lens within circular apertures corresponding to the relevant physical scales, $r_{\text{ap}} = r_e$, $r_e/2$, and θ_E , we first integrate the best-fit κ model (Table 2) within each aperture to obtain the enclosed total mass, $M_{\text{lensing}}(< r_{\text{ap}})$. We then integrate the Sérsic light profile over the same aperture to derive the enclosed light fraction, f_{\star} , defined as the fraction of the total luminosity enclosed within r_{ap} . Assuming that stellar mass follows the observed light, we use this fraction to infer the enclosed stellar mass within the same aperture. The dark-matter fraction is then calculated by comparing the enclosed total and stellar masses. The resulting values are summarized in Table 5.

5.2. Comparison with Previous Work

To put our system into context, we constructed a compilation of previously known strong lenses produced by close galaxy pairs. The details—including 14 projected lens-lens separations and the relevant references—are summarized

Table 6. Fourteen strong-lens systems with close galaxy-pair deflectors (projected separations of $\sim 1\text{--}50h^{-1}$ kpc). For consistency, the projected separations in kpc are recomputed under the cosmology used in this work. The systems are sorted in ascending order of projected lens–lens separation (kpc).

System	Projected lens–lens separation	z_d	References
PMN J0134–0931	$0''.385$ (2.84 kpc)	0.76	C. R. Keeton & J. N. Winn (2003)
HSC J0233–0205	$0''.513$ (3.83 kpc)	0.79	This Work
2M1310–1714	$0''.91$ (3.99 kpc)	0.293	J. R. Lucey et al. (2018); F. Dux et al. (2025)
SDSS J1011+0143	$0''.88$ (4.19 kpc)	0.331	Y. Shu et al. (2016)
B1608+656	$0''.73$ (4.99 kpc)	0.6304	S. H. Suyu et al. (2010)
HE 0230–2130	$1''.02$ (6.38 kpc)	0.523	S. Ertl et al. (2024)
SDSS J1459–0055	$1''.2$ (7.88 kpc)	0.577	J. P. Willis et al. (2005)
SDSS J1405+0959	$1''.68$ (11.72 kpc)	0.66	C. E. Rusu et al. (2014)
MG J0414+0534	$1''.509$ (11.96 kpc)	0.9584	J. L. Tonry & C. S. Kochanek (1999)
DES J0408–5354	$3''.23$ (21.54 kpc)	0.597	A. Agnello et al. (2017)
SL2S J08544–0121	$5''.289$ (26.27 kpc)	0.3530	S. H. Suyu & A. Halkola (2010)
CASSOWARY5	$5''.34$ (28.16 kpc)	0.388	C. Grillo & L. Christensen (2011)
CLASS B1127+385	$0''.60$ (–)	–	L. V. E. Koopmans et al. (1999)
PS J0630–1201	$1''.08$ (–)	–	F. Ostrovski et al. (2018)

in Table 6. From this table, we find that HSC J0233–0205 has the second-highest redshift and the second-smallest projected lens–lens separation among the compiled systems.

Because our interest of the dark-matter fraction, we compare our measurements to those reported in previous studies. This comparison includes lenses produced by field galaxies—specifically those from the Strong Lensing Legacy Survey (SL2S; A. J. Ruff et al. 2011) and the Sloan Lens ACS Survey (SLACS; M. W. Auger et al. 2010)—as well as the close galaxy-pair lenses listed in Table 6. Among the latter, however, only C. Grillo & L. Christensen (2011) explicitly reported projected dark-matter fractions for both deflectors.

First, we find that the trend whereby more massive lens galaxies exhibit larger dark-matter fractions within both $r_e/2$ and r_e —i.e., higher $f_{\text{dm}}(< r_e/2)$ and $f_{\text{dm}}(< r_e)$ —is broadly consistent with previous results, including those from SLACS, SL2S, and the CASSOWARY system studied by C. Grillo & L. Christensen (2011). Second, our measured $f_{\text{dm}}(< r_e/2)$ values are consistent with those reported for SLACS and SL2S lenses, suggesting comparable inner mass budgets to field early-type lens galaxies. Figure 6 shows the direct comparison between our results and the SL2S sample.

Finally, a significant discrepancy emerges when comparing our $f_{\text{dm}}(< r_e)$ measurements to those of CASSOWARY5 (C. Grillo & L. Christensen 2011). For our system, we find lower $f_{\text{dm}}(< r_e)$ values of $57\% \pm 11\%$ (lens1) and $70\% \pm 6\%$ (lens2), whereas C. Grillo & L. Christensen (2011) reported $\sim 80\% \pm 10\%$ for both lenses in a galaxy group containing two deflectors separated by ~ 28 kpc. This tension is unlikely to be resolved by IMF assumptions: we adopt a Chabrier IMF, while C. Grillo & L. Christensen (2011) assumed a Salpeter IMF. Because a Salpeter IMF implies a larger stellar mass M_* and therefore a smaller inferred $f_{\text{dm}}(< r_e)$, converting their stellar masses to a Chabrier basis would, if anything, further increase the discrepancy.

A plausible explanation is that the lenses analyzed by C. Grillo & L. Christensen (2011) are substantially more massive than ours. After converting to a Chabrier IMF (using a scale factor of 1.4), their two lenses have stellar masses of $\sim 2.2 \times 10^{11} M_\odot$ and $\sim 4.2 \times 10^{11} M_\odot$, whereas our lenses have $M_* \approx 0.8 \times 10^{11} M_\odot$ and $1.5 \times 10^{11} M_\odot$. Indeed, C. Grillo & L. Christensen (2011) described their system as “dark-matter rich” relative to SLACS field early-type galaxies and attributed this difference to the overdense environment and a more dark-matter–concentrated mass distribution.

5.3. Limitations and Future Plans

The current data impose important limitations, and several aspects of this system could be substantially improved with higher-quality observations.

1. At present, we only have ground-based HSC imaging and lack high-resolution data. This prevents a direct search for merger signatures—such as tidal tails, disturbed isophotes, or faint satellites—associated with lens1 and lens2.
2. Although our modeling favors lens1 and lens2 being at the same redshift—supported, for example, by their similar colors and by the fact that a single-redshift assumption already provides an adequate description of the data—we currently only have a combined spectrum of lens1+lens2. We therefore cannot yet unambiguously confirm that the two galaxies share the same redshift.
3. Our stellar-mass constraints are based on rest-frame wavelengths of roughly $\sim 266\text{--}545\text{nm}$. The absence of near-infrared photometry may thus bias the inferred stellar masses and increases the associated uncertainties.

Taken together, these considerations highlight the importance of deeper and higher-quality follow-up observations. High-resolution imaging (e.g., with space-based facilities) would be essential for identifying merger features and improving the robustness of the lens–light decomposition. Moreover, such data would enable a search for potential spatial offsets between the luminous components and the dark-matter mass distribution (Y. Shu et al. 2016), providing an additional probe of the dynamical state of the system. Finally, spatially resolved or separate spectroscopy would provide a definitive test of whether the two deflectors indeed lie at the same redshift.

6. CONCLUSIONS

To summarize, we present the spectroscopic confirmation and lens modeling of the strong-lensing system HSC J0233–0205, which is produced by a close galaxy pair with a projected separation of 3.8 kpc and has an overall Einstein radius of $1''.680 \pm 0''.003$. P200/DBSP spectroscopy places the deflector and source at redshifts of $z_d = 0.790 \pm 0.022$ and $z_s = 2.160 \pm 0.001$, respectively. Our modeling shows that three source components are required to reproduce the observed lensed morphology. Among the close galaxy-pair lenses reported in the literature, this system is notable for being the second-highest-redshift example currently known and the one with the second-smallest projected separation.

By jointly fitting the five-band HSC imaging data (g, r, i, z, y), we measure Einstein radii of $0''.669 \pm 0''.002$ and $0''.735 \pm 0''.002$ for the two lens galaxies, separated by $0''.513$ (i.e., ~ 3.832 kpc). The total mass enclosed within the critical curve is $M_{\text{lensing, total}} = (1.107 \pm 0.008) \times 10^{12} M_\odot$. From SED fitting with CIGALE, we infer stellar masses of $M_{*, \text{lens1}} = (8.548 \pm 2.128) \times 10^{10} M_\odot$ and $M_{*, \text{lens2}} = (1.525 \pm 0.295) \times 10^{11} M_\odot$, implying a projected dark-matter fraction within the critical curve of $82\% \pm 4\%$. For the individual lenses, the projected dark-matter fractions within the z -band effective radii are $57\% \pm 11\%$ (lens1) and $70\% \pm 6\%$ (lens2). These results indicate that HSC J0233–0205 has the second-highest redshift and the second-smallest projected lens–lens separation among known strong lenses produced by close galaxy pairs, and it is the second such system for which the dark-matter fraction has been explicitly measured.

In the near future, missions such as Euclid (Euclid Collaboration et al. 2025) and Chinese Space Station Telescope (CSST; CSST Collaboration et al. 2026) are expected to discover many more strong-lensing systems produced by close galaxy pairs, providing valuable constraints on galaxy-merger physics and the dark-matter properties of lens galaxies.

7. ACKNOWLEDGMENTS

Z.H. acknowledges support from the National Natural Science Foundation of China (Grant No. 12403104). This research uses data obtained through the Telescope Access Program (TAP), which has been funded by the TAP association, including Centre for Astronomical Mega-Science CAS(CAMS), XMU, PKU, THU, USTC, NJU, YNU, and SYSU. We thank Houzun Chen for insightful discussions.

The Hyper Suprime-Cam (HSC) collaboration includes the astronomical communities of Japan and Taiwan, and Princeton University. The HSC instrumentation and software were developed by the National Astronomical Observatory of Japan (NAOJ), the Kavli Institute for the Physics and Mathematics of the Universe (Kavli IPMU), the University of Tokyo, the High Energy Accelerator Research Organization (KEK), the Academia Sinica Institute for Astronomy and Astrophysics in Taiwan (ASIAA), and Princeton University. Funding was contributed by the FIRST program from Japanese Cabinet Office, the Ministry of Education, Culture, Sports, Science and Technology (MEXT), the Japan Society for the Promotion of Science (JSPS), Japan Science and Technology Agency (JST), the Toray Science Foundation, NAOJ, Kavli IPMU, KEK, ASIAA, and Princeton University.

Based [in part] on data collected at the Subaru Telescope and retrieved from the HSC data archive system, which is operated by Subaru Telescope and Astronomy Data Center at National Astronomical Observatory of Japan.

REFERENCES

- Agnello, A., Lin, H., Buckley-Geer, L., et al. 2017, *MNRAS*, 472, 4038, doi: [10.1093/mnras/stx2242](https://doi.org/10.1093/mnras/stx2242)
- Aihara, H., Arimoto, N., Armstrong, R., et al. 2018, *PASJ*, 70, S4, doi: [10.1093/pasj/psx066](https://doi.org/10.1093/pasj/psx066)
- Aihara, H., AlSayyad, Y., Ando, M., et al. 2022, *PASJ*, 74, 247, doi: [10.1093/pasj/psab122](https://doi.org/10.1093/pasj/psab122)
- Astropy Collaboration, Price-Whelan, A. M., Lim, P. L., et al. 2022, *ApJ*, 935, 167, doi: [10.3847/1538-4357/ac7c74](https://doi.org/10.3847/1538-4357/ac7c74)
- Auger, M. W., Treu, T., Bolton, A. S., et al. 2010, *ApJ*, 724, 511, doi: [10.1088/0004-637X/724/1/511](https://doi.org/10.1088/0004-637X/724/1/511)
- Birrer, S., & Amara, A. 2018, *Physics of the Dark Universe*, 22, 189, doi: [10.1016/j.dark.2018.11.002](https://doi.org/10.1016/j.dark.2018.11.002)
- Bolton, A. S., Burles, S., Koopmans, L. V. E., et al. 2008, *ApJ*, 682, 964, doi: [10.1086/589327](https://doi.org/10.1086/589327)
- Bolton, A. S., Brownstein, J. R., Kochanek, C. S., et al. 2012, *ApJ*, 757, 82, doi: [10.1088/0004-637X/757/1/82](https://doi.org/10.1088/0004-637X/757/1/82)
- Boquien, M., Burgarella, D., Roehly, Y., et al. 2019, *A&A*, 622, A103, doi: [10.1051/0004-6361/201834156](https://doi.org/10.1051/0004-6361/201834156)
- Bruzual, G., & Charlot, S. 2003, *MNRAS*, 344, 1000, doi: [10.1046/j.1365-8711.2003.06897.x](https://doi.org/10.1046/j.1365-8711.2003.06897.x)
- Chabrier, G. 2003, *PASP*, 115, 763, doi: [10.1086/376392](https://doi.org/10.1086/376392)
- Chae, K.-H., Biggs, A. D., Blandford, R. D., et al. 2002, *PhRvL*, 89, 151301, doi: [10.1103/PhysRevLett.89.151301](https://doi.org/10.1103/PhysRevLett.89.151301)
- Charlot, S., & Fall, S. M. 2000, *ApJ*, 539, 718, doi: [10.1086/309250](https://doi.org/10.1086/309250)
- CSST Collaboration, Gong, Y., Miao, H., et al. 2026, *Science China Physics, Mechanics, and Astronomy*, 69, 239501, doi: [10.1007/s11433-025-2809-0](https://doi.org/10.1007/s11433-025-2809-0)
- Dux, F., Millon, M., Galan, A., et al. 2025, *A&A*, 697, A139, doi: [10.1051/0004-6361/202553807](https://doi.org/10.1051/0004-6361/202553807)
- Er, X., Li, G., Mao, S., & Cao, L. 2013, *MNRAS*, 430, 1423, doi: [10.1093/mnras/stt012](https://doi.org/10.1093/mnras/stt012)
- Ertl, S., Schuldt, S., Suyu, S. H., et al. 2024, *A&A*, 685, A15, doi: [10.1051/0004-6361/202347689](https://doi.org/10.1051/0004-6361/202347689)
- Euclid Collaboration, Mellier, Y., Abdurro'uf, et al. 2025, *A&A*, 697, A1, doi: [10.1051/0004-6361/202450810](https://doi.org/10.1051/0004-6361/202450810)
- Geng, S., Grespan, M., Thuruthipilly, H., et al. 2025, *A&A*, 694, A196, doi: [10.1051/0004-6361/202451894](https://doi.org/10.1051/0004-6361/202451894)
- Granata, G., Bergamini, P., Grillo, C., et al. 2023, *A&A*, 679, A124, doi: [10.1051/0004-6361/202347521](https://doi.org/10.1051/0004-6361/202347521)
- Grillo, C., & Christensen, L. 2011, *MNRAS*, 418, 929, doi: [10.1111/j.1365-2966.2011.19544.x](https://doi.org/10.1111/j.1365-2966.2011.19544.x)
- Harris, C. R., Millman, K. J., van der Walt, S. J., et al. 2020, *Nature*, 585, 357, doi: [10.1038/s41586-020-2649-2](https://doi.org/10.1038/s41586-020-2649-2)
- He, Z., Chen, Q., Deng, L., et al. 2025, arXiv e-prints, arXiv:2501.08541, doi: [10.48550/arXiv.2501.08541](https://doi.org/10.48550/arXiv.2501.08541)
- He, Z., Er, X., Long, Q., et al. 2020, *MNRAS*, 497, 556, doi: [10.1093/mnras/staa1917](https://doi.org/10.1093/mnras/staa1917)
- Huang, X., Storfer, C., Gu, A., et al. 2021, *ApJ*, 909, 27, doi: [10.3847/1538-4357/abd62b](https://doi.org/10.3847/1538-4357/abd62b)
- Hutchinson, T. A., Bolton, A. S., Dawson, K. S., et al. 2016, *AJ*, 152, 205, doi: [10.3847/0004-6256/152/6/205](https://doi.org/10.3847/0004-6256/152/6/205)
- Jaelani, A. T., More, A., Oguri, M., et al. 2020, *Monthly Notices of the Royal Astronomical Society*, 495, 1291, doi: [10.1093/mnras/staa1062](https://doi.org/10.1093/mnras/staa1062)
- Jones, T. A., Swinbank, A. M., Ellis, R. S., Richard, J., & Stark, D. P. 2010, *MNRAS*, 404, 1247, doi: [10.1111/j.1365-2966.2010.16378.x](https://doi.org/10.1111/j.1365-2966.2010.16378.x)
- Keeton, C. R., & Winn, J. N. 2003, *ApJ*, 590, 39, doi: [10.1086/374833](https://doi.org/10.1086/374833)
- Kneib, J.-P., & Natarajan, P. 2011, *A&A Rv*, 19, 47, doi: [10.1007/s00159-011-0047-3](https://doi.org/10.1007/s00159-011-0047-3)
- Koopmans, L. V. E., Treu, T., Bolton, A. S., Burles, S., & Moustakas, L. A. 2006, *ApJ*, 649, 599, doi: [10.1086/505696](https://doi.org/10.1086/505696)
- Koopmans, L. V. E., de Bruyn, A. G., Marlow, D. R., et al. 1999, *MNRAS*, 303, 727, doi: [10.1046/j.1365-8711.1999.02342.x](https://doi.org/10.1046/j.1365-8711.1999.02342.x)
- Li, R., Shu, Y., & Wang, J. 2018, *MNRAS*, 480, 431, doi: [10.1093/mnras/sty1813](https://doi.org/10.1093/mnras/sty1813)
- Li, R., Napolitano, N. R., Spiniello, C., et al. 2021, *ApJ*, 923, 16, doi: [10.3847/1538-4357/ac2df0](https://doi.org/10.3847/1538-4357/ac2df0)
- Li, T., Collett, T. E., Krawczyk, C. M., & Enzi, W. 2024, *MNRAS*, 527, 5311, doi: [10.1093/mnras/stad3514](https://doi.org/10.1093/mnras/stad3514)
- Lucey, J. R., Schechter, P. L., Smith, R. J., & Anguita, T. 2018, *MNRAS*, 476, 927, doi: [10.1093/mnras/sty243](https://doi.org/10.1093/mnras/sty243)
- Marian, V., Ziegler, B., Kuchner, U., & Verdugo, M. 2018, *A&A*, 617, A34, doi: [10.1051/0004-6361/201832750](https://doi.org/10.1051/0004-6361/201832750)
- McCully, C., Crawford, S., Kovacs, G., et al. 2018, *astropy/astrocrappy: v1.0.5 Zenodo Release, v1.0.5 Zenodo*, doi: [10.5281/zenodo.1482019](https://doi.org/10.5281/zenodo.1482019)
- Meneghetti, M., Davoli, G., Bergamini, P., et al. 2020, *Science*, 369, 1347, doi: [10.1126/science.aax5164](https://doi.org/10.1126/science.aax5164)
- Natarajan, P., Williams, L. L. R., Bradač, M., et al. 2024, *SSRv*, 220, 19, doi: [10.1007/s11214-024-01051-8](https://doi.org/10.1007/s11214-024-01051-8)
- Nishizawa, A. J., Hsieh, B.-C., Tanaka, M., & Takata, T. 2020, arXiv e-prints, arXiv:2003.01511, doi: [10.48550/arXiv.2003.01511](https://doi.org/10.48550/arXiv.2003.01511)
- Oguri, M., Inada, N., Strauss, M. A., et al. 2012, *AJ*, 143, 120, doi: [10.1088/0004-6256/143/5/120](https://doi.org/10.1088/0004-6256/143/5/120)
- Oke, J. B., & Gunn, J. E. 1982, *PASP*, 94, 586, doi: [10.1086/131027](https://doi.org/10.1086/131027)
- Ostrovski, F., Lemon, C. A., Auger, M. W., et al. 2018, *MNRAS*, 473, L116, doi: [10.1093/mnrasl/slx173](https://doi.org/10.1093/mnrasl/slx173)
- Ruff, A. J., Gavazzi, R., Marshall, P. J., et al. 2011, *ApJ*, 727, 96, doi: [10.1088/0004-637X/727/2/96](https://doi.org/10.1088/0004-637X/727/2/96)

- Rusu, C. E., Oguri, M., Minowa, Y., et al. 2014, MNRAS, 444, 2561, doi: [10.1093/mnras/stu1621](https://doi.org/10.1093/mnras/stu1621)
- Schuldt, S., Suyu, S. H., Cañameras, R., et al. 2023, A&A, 673, A33, doi: [10.1051/0004-6361/202244534](https://doi.org/10.1051/0004-6361/202244534)
- Sheu, W., Shajib, A. J., Treu, T., et al. 2025, MNRAS, 541, 1, doi: [10.1093/mnras/staf976](https://doi.org/10.1093/mnras/staf976)
- Shu, Y., Bolton, A. S., Moustakas, L. A., et al. 2016, ApJ, 820, 43, doi: [10.3847/0004-637X/820/1/43](https://doi.org/10.3847/0004-637X/820/1/43)
- Shu, Y., Brownstein, J. R., Bolton, A. S., et al. 2017, ApJ, 851, 48, doi: [10.3847/1538-4357/aa9794](https://doi.org/10.3847/1538-4357/aa9794)
- Sonnenfeld, A., Chan, J. H. H., Shu, Y., et al. 2018, PASJ, 70, S29, doi: [10.1093/pasj/psx062](https://doi.org/10.1093/pasj/psx062)
- Suyu, S. H. 2012, MNRAS, 426, 868, doi: [10.1111/j.1365-2966.2012.21661.x](https://doi.org/10.1111/j.1365-2966.2012.21661.x)
- Suyu, S. H., & Halkola, A. 2010, A&A, 524, A94, doi: [10.1051/0004-6361/201015481](https://doi.org/10.1051/0004-6361/201015481)
- Suyu, S. H., Marshall, P. J., Auger, M. W., et al. 2010, ApJ, 711, 201, doi: [10.1088/0004-637X/711/1/201](https://doi.org/10.1088/0004-637X/711/1/201)
- Swinbank, A. M., Bower, R. G., Smith, G. P., et al. 2007, MNRAS, 376, 479, doi: [10.1111/j.1365-2966.2007.11454.x](https://doi.org/10.1111/j.1365-2966.2007.11454.x)
- Tanaka, M., Coupon, J., Hsieh, B.-C., et al. 2018, PASJ, 70, S9, doi: [10.1093/pasj/psx077](https://doi.org/10.1093/pasj/psx077)
- Tonry, J. L., & Kochanek, C. S. 1999, AJ, 117, 2034, doi: [10.1086/300834](https://doi.org/10.1086/300834)
- Treu, T. 2010, ARA&A, 48, 87, doi: [10.1146/annurev-astro-081309-130924](https://doi.org/10.1146/annurev-astro-081309-130924)
- Turner, E. L., Ostriker, J. P., & Gott, III, J. R. 1984, ApJ, 284, 1, doi: [10.1086/162379](https://doi.org/10.1086/162379)
- vanderWel, A., Franx, M., van Dokkum, P. G., et al. 2014, ApJ, 788, 28, doi: [10.1088/0004-637X/788/1/28](https://doi.org/10.1088/0004-637X/788/1/28)
- Virtanen, P., Gommers, R., Oliphant, T. E., et al. 2020, Nature Methods, 17, 261, doi: [10.1038/s41592-019-0686-2](https://doi.org/10.1038/s41592-019-0686-2)
- Vulcani, B., Bamford, S. P., Häußler, B., et al. 2014, MNRAS, 441, 1340, doi: [10.1093/mnras/stu632](https://doi.org/10.1093/mnras/stu632)
- Wes McKinney. 2010, in Proceedings of the 9th Python in Science Conference, ed. Stéfan van der Walt & Jarrod Millman, 56 – 61, doi: [10.25080/Majora-92bf1922-00a](https://doi.org/10.25080/Majora-92bf1922-00a)
- Willis, J. P., Hewett, P. C., & Warren, S. J. 2005, MNRAS, 363, 1369, doi: [10.1111/j.1365-2966.2005.09533.x](https://doi.org/10.1111/j.1365-2966.2005.09533.x)